I&EC research
Industrial & Engineering Chemistry Research

Article

Cite This: Ind. Eng. Chem. Res. 2017, 56, 15131−15142

pubs.acs.org/IECR

Precipitating Characteristics of Potassium Bicarbonate Using Concentrated Potassium Carbonate Solvent for Carbon Dioxide Capture. Part 2: Crystal Growth

Yue Wu,[†,‡] Lefu Tao,[†,‡] Fan Wu,[†] Nouman R. Mirza,[†,‡] Geoffrey W. Stevens,[†,‡] and Kathryn A. Mumford*[,†,‡]

[†]Department of Chemical and Biomolecular Engineering, The University of Melbourne, Victoria, Australia
[‡]Peter Cook Centre for CCS Research, The University of Melbourne, Victoria, Australia

ABSTRACT: Crystallization kinetics of potassium bicarbonate in the potassium carbonate (K_2CO_3)−potassium bicarbonate ($KHCO_3$)−water (H_2O) ternary solvent system were estimated using focused beam reflectance measurement (FBRM) in unseeded batch cooling experiments. Two groups of experiments including apparent K_2CO_3 concentrations of 35 and 40 wt %, both with 0.4 loading, at different constant cooling rates were conducted. $KHCO_3$ was the only precipitate in the ternary system. The concentration of $KHCO_3$ measured by autotitration and chord length distribution collected from FBRM were used to estimate the parameters required for the primary nucleation, secondary nucleation, and growth rate models through mass balance, population balance using the method of moments, and least-squares minimization in MATLAB. The solubility of the ternary solvent system was successfully predicted using the regressed electrolyte nonrandom two-liquids (ENRTL) activity model in Aspen Plus. The crystallization of $KHCO_3$ was impacted by $KHCO_3$ supersaturation and K_2CO_3 concentration. Primary nucleation was found to dominate the system including both homogeneous and heterogeneous nucleation, whereas secondary nucleation was inhibited to a great extent. The model developed was able to predict the average particle size within 20%, the results obtained from the model were consistent with the conclusion that primary nucleation dominates the K_2CO_3−$KHCO_3$−H_2O solvent system.

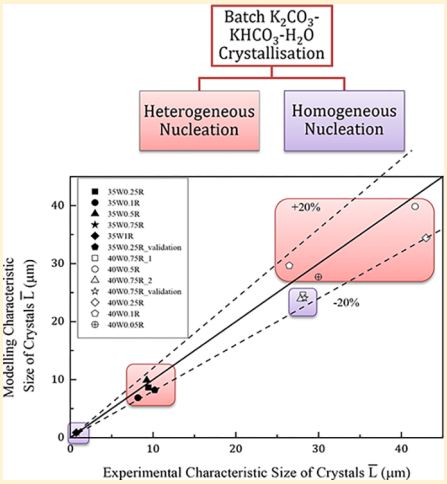

1. INTRODUCTION

Potassium carbonate (K_2CO_3) solvent has traditionally been applied to remove carbon dioxide (CO_2) from synthesis gas produced via the Fischer−Tropsch process. Here, the synthesis gas is at high pressure (>10 bar) and high temperature; this is known as the Benson and Field hot K_2CO_3 process.[1] Presently, K_2CO_3 solvent has been gaining momentum for application in post-combustion capture processes that require capture at relatively low pressures and low temperatures. Compared to monoethanolamine (MEA), which is regarded as the industrial benchmark for CO_2 capture in post-combustion processes, K_2CO_3 solvent may have great potential as MEA is highly degradable, toxic, and corrosive, and it also requires a large amount of energy for regeneration.[2−4] However, the absorption of CO_2 using pure K_2CO_3 solvent exhibits slow reaction kinetics. In order to improve CO_2 absorption efficiency, a variety of promoters (including inorganic promoters such as arsenite, boric acid, and vanadate), organic promoters (such as amines and amino acid salts), and enzymes have been added to K_2CO_3 in an attempt to increase reaction kinetics.[5,6] Another potential improvement to the K_2CO_3 solvent may be inducing a phase change in the solvent system to increase CO_2 absorption capacity. In this method, CO_2 is absorbed using concentrated K_2CO_3 solvent, and the product, potassium bicarbonate ($KHCO_3$), may be precipitated out from the solvent system. If the solid precipitate is removed quickly, the equilibrium of the concentrated K_2CO_3 solvent system may be altered, which increases CO_2 absorption capacity.[7] This method may also reduce the regeneration energy requirement, since the water content in the solvent is reduced.[8] The overall reaction for the phase change process is shown in reaction R1.

$$CO_2(g) + K_2CO_3(aq) + H_2O(l) \rightleftharpoons 2KHCO_3(aq) \rightleftharpoons 2KHCO_3(s) \quad \text{(R1)}$$

The introduction of solid precipitation may also result in some operational issues, such as blockage and fouling in process equipment, especially in packed columns. Therefore, the investigation of the crystallization behavior in K_2CO_3−$KHCO_3$−H_2O ternary solvent system is important. Ye et al.[9] from the University of Illinois at Urbana−Champaign has studied the crystallization kinetics of $KHCO_3$ in concentrated K_2CO_3 systems in a mixed-suspension, mixed-product removal (MSMPR) reactor, which was a continuous crystallization process at a laboratory scale.

Received: September 1, 2017
Revised: November 30, 2017
Accepted: November 30, 2017
Published: November 30, 2017

DOI: 10.1021/acs.iecr.7b03637
Ind. Eng. Chem. Res. 2017, 56, 15131−15142

Compared to the continuous crystallization process, batch crystallization is regarded as a relatively simple unit operation, which can be flexible and cost-effective to retrofit and integrate into the existing process, and remains of high interest.[10] Moreover, the investigation of crystallization kinetics in a batch cooling system can collect more useful information with optimized control strategies, because all kinetic parameters are time-dependent. For example, batch crystallization with accurate temperature control is of particular interest due to temperature effects on precipitating behavior and its importance to the design and operation of a CO_2 absorber. The primary nucleation of $KHCO_3$ in an unseeded batch crystallizer using both a metastable zone width method and a pseudo-induction-time method has been previously investigated.[11] The experiment was conducted using focused beam reflectance measurement (FBRM), which is an effective process analytical technique, with precise temperature control provided by an Optimax 1001 Workstation (Mettler−Toledo, CH). Previous work indicated that two regimes for primary nucleation existed and were dependent on the cooling rate. Heterogeneous nucleation occurred at low cooling rates (Region I), whereas homogeneous nucleation occurred at high cooling rates (Region II).[11] In this paper, these initial findings are further investigated through understanding of secondary nucleation and the growth kinetics of $KHCO_3$ precipitates in an unseeded batch crystallizer. Here, the precipitates that result from primary nucleation are considered as the seeds, providing sufficient crystal surfaces for secondary nucleation to occur. This secondary nucleation results in a significant increase in total particles. The growth of $KHCO_3$ crystals may also be used to determine the final particle size in the concentrated K_2CO_3 solvent.

2. EXPERIMENT AND METHOD

2.1. Chemicals and Instruments. Potassium bicarbonate (≥99.5% purity, Chem Supply), potassium carbonate ((≥99.5% purity, UCID) and ultrapure water (18.2 MΩ cm^{-1}, Elix Milipore) were used to prepare the K_2CO_3−$KHCO_3$−H_2O ternary solvent system without further purification. Sulfuric acid (98%, Science Supply) was used to prepare the 0.4 M standard sulfuric acid titrant to measure the concentration of $KHCO_3$ and K_2CO_3 in the ternary system. Ethanol (99.9%, Merck) was used to wash the precipitates after each experiment for imaging purposes.

An Optimax 1001 Workstation equipped with a 1000 mL glass reactor was used to control temperature and rotation speed. FRBM probe G400 (Mettler−Toledo, CH) was integrated with the Optimax 1001 Workstation to measure the in situ particle size distribution. Field-emission scanning electron microscopy (FESEM) (Philips, Model XL30 FEG, 2 kV beam) and optical microscopy (Prism Optical, SciTech, AU) were used to capture the images of the precipitates after precipitation completion. Metrohm 905 Titrando autotitrator (CH) was used to determine the concentration of $KHCO_3$ and K_2CO_3 in the ternary solvent system.

2.2. Experiment Setup. Two apparent K_2CO_3 concentrations (35 and 40 wt %), both with 0.4 CO_2 loading, were investigated over different cooling rates; the experimental design is shown in Table 1. Here, CO_2 loading is the product ($KHCO_3$) molar concentration in the K_2CO_3−$KHCO_3$−H_2O solvent system, representing the amount of CO_2 absorbed by the absorbent, divided by the concentration of K^+ ions and may be written as $[HCO_3^-]/[K^+]$.[12] The apparent K_2CO_3 concentration is defined as the concentration of K_2CO_3 when CO_2 loading is zero, because of the assumption that pure K_2CO_3 solvent is initially used.

Table 1. Experimental Design for Measuring Crystallization Kinetics

apparent K_2CO_3 concentration (wt %)	loading	nucleation region	constant cooling rate (°C/min)	experiment No.
35	0.4	Region I	0.1	35W0.1R
35	0.4	Region I	0.25	35W0.25R
35	0.4	Region I	0.5	35W0.5R
35	0.4	Region II	0.75	35W0.75R
35	0.4	Region II	1	35W1R
40	0.4	Region I	0.05	40W0.05R
40	0.4	Region I	0.1	40W0.1R
40	0.4	Region I	0.25	40W0.25R
40	0.4	Region I	0.5	40W0.5R
40	0.4	Region II	0.75	40W0.75R_1
40	0.4	Region II	0.75	40W0.75R_2

A large volume of 800 mL solution was prepared for each group of experiments in order to reduce the stochastic nature of cooling crystallization experiments.[13] The K_2CO_3−$KHCO_3$−H_2O solvent of the selected concentration was initially heated to 85 °C for 15 min to ensure that there were no solids present. The group of solutions with an apparent K_2CO_3 concentration of 35 wt % then were cooled to 60 °C, whereas the group with an apparent K_2CO_3 concentration of 40 wt % were cooled to 75 °C, where the set temperatures are slightly higher (∼5 °C) than their supersaturated temperatures. Both groups were maintained at their set temperature for 30 min, and then cooled to 25 °C and maintained for another 30 min at the preset cooling rates shown in Table 1. The impeller rotation rate for all experiments was maintained at 400 revolutions per minute (400 RPM), so that air bubbles introduced from high-speed turbulence did not impact the FBRM probe readings.

In order to monitor the concentration change of $KHCO_3$ and K_2CO_3 in the system during the cooling procedure, a method that was similar to that developed by Khateeb was used.[14] Two 2 mL of samples were withdrawn at set time intervals from the crystallizer using a nylon syringe filter (13 mm × 0.45 μm, Science Supply), and the samples were then titrated based on the different pK_a values exhibited by $KHCO_3$ and K_2CO_3 to measure their concentrations using a Metrohm 905 Titrando autotitrator.[15] The scan time interval of the FBRM was set at 10 s and the display mode of size distribution was set as "Macro", because of the transparency of crystal surfaces. More details about titration principles and the settings of the Optimax 1001 Workstation and FRBM can be found in our previous work.[11] When the experiment ended, the crystals were immediately filtered and washed using ethanol, and finally dried in a vacuum oven prior to imaging via optical microscopy and SEM. The experimental setup is presented in Figure 1.

3. MODEL

According to the previous studies of Ye and Wu,[9,11] $KHCO_3$ crystals are the only precipitate in the K_2CO_3−$KHCO_3$−H_2O solvent system under post-combustion CO_2 capture conditions. To adequately describe the crystallization behaviors along with the kinetics, this section discusses the mathematical model of $KHCO_3$ solid precipitation including primary nucleation, secondary nucleation, and crystal growth in an unseeded batch cooling crystallizer, based on the population balance equations

DOI: 10.1021/acs.iecr.7b03637
Ind. Eng. Chem. Res. 2017, 56, 15131−15142

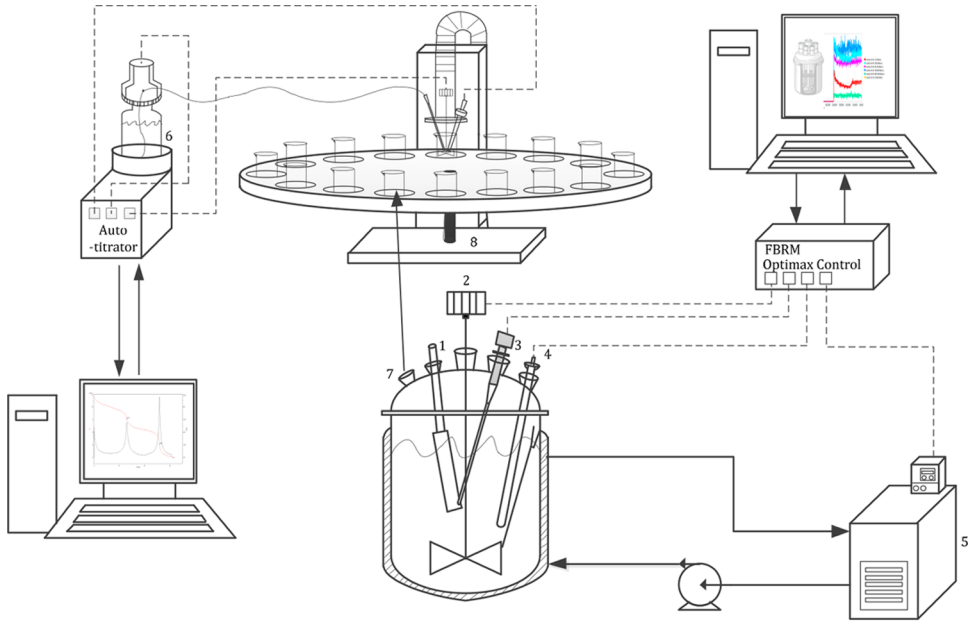

1 – Baffle blade, 2 – Impeller, 3 – FBRM, 4 – Temperature sensor, 5 – Water bath, 6 – 0.4M Sulfuric acid, 7 – Sampling port, 8 – Titrator workstation

Figure 1. Experimental setup for measuring $KHCO_3$ crystal kinetics.

(PBEs). The kinetic parameters were then estimated using least-squares regression.

3.1. Crystallization Kinetics. PBEs are effective modeling tools that are widely applied into the engineering field of dispersed media such as crystallization, biotechnologies, novel solvent extraction processes, and powder technologies.[16−18] To simplify a laboratory-scale batch crystallization process, a well-mixed crystallizer is generally assumed. This means the temperature and concentration throughout the crystallizer is the same at a given time. In addition, there is no spatial variation of particle size distribution at a given time.[19] If only the characteristic dimension of the crystals is considered, and there is no agglomeration or breakage observed during the crystallization process, the PBE may be described as a partial differential equation (PDE):

$$\frac{\partial n(t, L)}{\partial t} + \frac{\partial [G(t)n(t, L)]}{\partial L} = 0 \tag{1}$$

where $n(t, L)$ is the population density of $KHCO_3$ crystals ((number of crystals)/m/m^3 of solvent), t the time (min), $G(t)$ the crystal growth rate (m/min), and L the characteristic length of $KHCO_3$ crystals (m).

In most published work related to batch crystallization, the growth rate of crystals is assumed to follow McCabe's law. This law states that the growth rate G is independent of crystal size and is only dependent on the degree of supersaturation.[18] If this is assumed, eq 1 can be rewritten as

$$\frac{\partial n(t, L)}{\partial t} + G(t)\frac{\partial n(t, L)}{\partial L} = 0 \tag{2}$$

For an unseeded batch cooling crystallization experiment, the boundary conditions of eq 2 are given by

$$n(t, 0) = \frac{J(t)}{G(t)} \tag{3}$$

$$n(0, L) = 0 \tag{4}$$

where $J(t)$ is the nucleation rate ((number of crystals)/(m^3 of solvent)/min).

Since the cooling process is temperature-sensitive, the growth rate of $KHCO_3$ crystals can be expressed as a semiempirical power law, which is defined by

$$G(t) = k_g A^g \tag{5}$$

where k_g ((m/min) (m^3/kmol)^g) and g are the empirical parameters to be estimated. A may be expressed as absolute supersaturation ($C(t) - C^*(T)$) or supersaturation ratio ($C(t)/C^*(T)$). $C(t)$ and $C^*(T)$ (kmol/m^3) are the concentration and the corresponding saturated concentration of $KHCO_3$ at a given time. Here, we chose absolute supersaturation, because the supersaturation ratio ($S(t) = C(t)/C^*(T)$) for growth kinetics is relatively small under the investigated range of $KHCO_3$ concentration.

Generally solving PDEs is time-consuming and requires an efficient algorithm. This is particularly important when fitting multiple parameters to experimental data. Here, the method of moments is used by multiplying L^j ($j = 0, 1, 2, ...$) on both sides of eq 2, which transforms the PDEs to ordinary differential equations (ODEs) in terms of moments,[20] which is shown as

$$\frac{d\mu_0}{dt} = J(t) \quad (j = 0) \tag{6}$$

$$\frac{d\mu_j}{dt} = jG(t)\mu_{j-1} \quad (j \geq 1) \tag{7}$$

Here, the jth moment is defined as

$$\mu_j = \int_0^\infty n(t, L)L^j \, dL \tag{8}$$

Regarding the particle size distribution in the system, the zeroth, first, second, and third moment μ_0 ((number of crystals)/(m^3 of solvent)), μ_1 ((number of crystals) m/(m^3 of solvent)), μ_2 ((number of crystals) m^2/(m^3 of solvent)), and

DOI: 10.1021/acs.iecr.7b03637
Ind. Eng. Chem. Res. 2017, 56, 15131−15142

μ_3 ((number of crystals) $m^3/(m^3$ of solvent)) have specific physical meanings, which are proportional to the total number, total length, total surface area, and total volume of the crystals, respectively.

The ODEs (eqs 6 and 7) are combined with a mass balance of the solute to constitute the overall mass balance of the batch crystallization process, which is given by

$$\frac{dC(t)}{dt} = -\rho_c k_v \frac{d\mu_3}{dt} = -3\rho_c k_v G \mu_2 \quad (9)$$

where ρ_c is the molar density of $KHCO_3$ (21.675 kmol/m^3), and k_v is a volumetric shape factor.

$KHCO_3$ crystals were found to have a hexagonal prism shape in our previous work.[11] Therefore, the volumetric shape factor (k_v) was defined by

$$Vol = k_v L^3 \quad (10)$$

where Vol (m^3) is the experimental volume of individual $KHCO_3$ crystal, with the assumption that the longest length of the $KHCO_3$ hexagonal prisms is the characteristic length L. Approximately 1200 particles with different sizes from all experiments were counted to calculate the average k_v value. From this, the value of k_v was set to be 0.16, which is similar with the shape factor of common hexagonal prism provided by Myerson.[21] Sample images are presented in Figure 2.

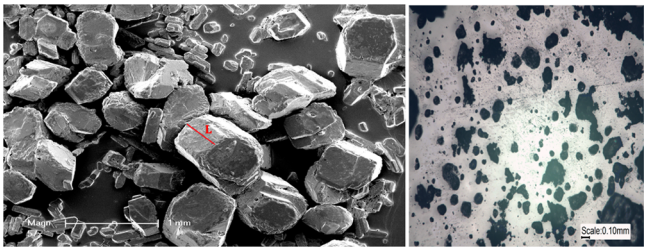

Figure 2. $KHCO_3$ crystals with the characteristic length in SEM (left) and optical microscopy (right) images.

Three crystallization behaviors—including primary nucleation, secondary nucleation, and crystal growth—occur simultaneously. As discussed, the crystal growth is given by eq 5. The nucleation kinetics may be described by eq 11:

$$J_1 = k_1 \exp\left(-\frac{B_1}{[\ln(S)]^2}\right) \quad (11)$$

$$J_2 = k_2 S^{b_2} \mu_2 \quad (12)$$

$$J = J_1 + J_2 \quad (13)$$

where J_1 ((number of crystals)/(m^3 of solvent)/min) is the primary nucleation rate, J_2 ((number of crystals)/(m^3 of solvent)/min) the secondary rate, k_1 ((number of crystals)/(m^3 of solvent)/min) the pre-exponential constant of primary nucleation, B_1 the exponential factor of primary nucleation, k_2 (1/m^2/min) the empirical constant of secondary nucleation, and b_2 the power factor of secondary nucleation.

Primary nucleation models were derived from classical nucleation theory (CNT), where B_1 in eq 11 is a combined effect of surface free energy and volume free energy.[22] The B_1 values for this work have been previously determined using Sangwal's CNT approach on the polythermal method.[11,23] The values were determined to be dependent both on cooling rate and on K_2CO_3 concentration, which, in turn, results in two different nucleation mechanisms (homogeneous and heterogeneous nucleation). The results are summarized in Table 2.

Table 2. B_1 Value of Primary Nucleation in the K_2CO_3–$KHCO_3$–H_2O Solvent System[a]

experiment No. (from Table 1)	apparent K_2CO_3 concentration (wt %)	loading	B_1
35W0.1R	35	0.4	0.00558
35W0.25R	35	0.4	0.00558
35W0.5R	35	0.4	0.00558
35W0.75R	35	0.4	0.00253
35W1R	35	0.4	0.00253
40W0.05R	40	0.4	0.00772
40W0.1R	40	0.4	0.00772
40W0.25R	40	0.4	0.00772
40W0.5R	40	0.4	0.00772
40W0.75R_1	40	0.4	0.00104
40W0.75R_2	40	0.4	0.00104

[a]Data taken from ref 11.

Equation 2 assumed that the $KHCO_3$ crystal growth follows McCabe's law, which is independent of crystal size. This assumption, in this case, can be justified by maximum population distribution provided by Wey and Estrin.[24] The maximum population distribution can be expressed as

$$\frac{dn(t, L_{max})}{dt} = -\left(n(t, L_{max})\frac{\partial G}{\partial L}\right)_{L_{max}} \quad (14)$$

$$\frac{dL_{max}}{dt} = G|_{L_{max}} + n(t, L_{max}) \cdot \left.\frac{\partial^2 G/\partial L^2}{\partial^2 n/\partial L^2}\right|_{L_{max}} \quad (15)$$

where $n(t, L_{max})$ is the population distribution at the maximum crystal size L_{max}.

Equations 14 and 15 represent the population distribution at the maximum crystal size changing with the time. If the crystal growth follows McCabe's law, $n(t, L_{max})$ remains unchanged with the increase of time, as $\partial G/\partial L = 0$. This relationship has been found in our work, which is shown in Figure 3.

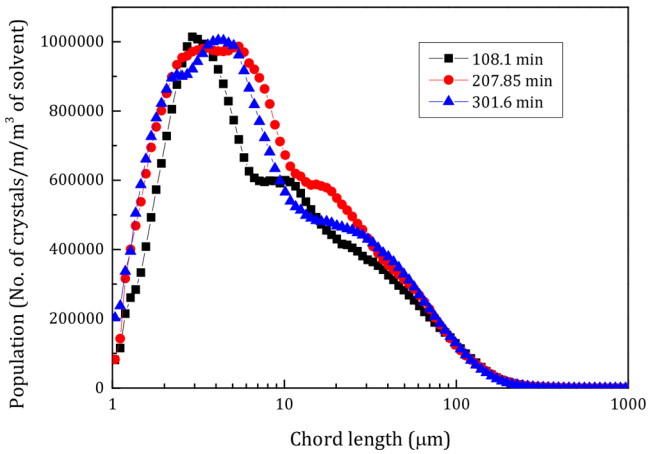

Figure 3. Population distribution (number weight) measured via FBRM (35W0.25R).

DOI: 10.1021/acs.iecr.7b03637
Ind. Eng. Chem. Res. 2017, 56, 15131–15142

Figure 3 shows the $KHCO_3$ crystals distribution in apparent 35 wt % K_2CO_3 solvent with 0.4 loading under a constant cooling rate of 0.25 °C. The population distribution in the form of chord length distribution was measured by FBRM, and smoothed using a 10-point adjacent averaging routine. The chord length is the distance between the edges of a particle when the high-speed spinning laser beam intersects the edges of the particle at two points in time. Although the chord length distribution is not the real particle size distribution, they are related and the total counts of chord length represent the total number of particles in the system.[25] This is also expected to be applicable in this case. Here, with the increase in the cooling time, the maximum chord length distribution $n_c(t, L_{max})$ does not increase or decrease. Instead, the entire distribution only shifts to the right. This also demonstrates that the growth of $KHCO_3$ crystals is size-independent. This feature was also found for the other groups of the experiments listed in Table 2.

3.2. Parameter Estimation. The moment equations for the population balance (eqs 6 and 7) coupled with mass balance (eq 9) and crystallization kinetics (eqs 5, 10−13) are used to fit the experimental data, which, in turn, can be used to estimate a set of crystallization kinetic parameters $\theta = [k_1, k_2, b_2, k_g, g]$. The value of B_1 was fixed, as indicated in Table 2.

The least-squares regression method is used for parameter estimation, and the objective function is given by

$$\min_\theta E = \sum_{j=1}^{N_{ex}} \sum_{i=1}^{N_s} \{[KHCO_3]^{sim}_{i(t,\theta)} - [KHCO_3]^{exp}_{i(t)}\}^2 \quad (16)$$

where $[KHCO_3]^{sim}_{i\,(t,\,\theta)}$ (kmol/m^3) is the simulated $KHCO_3$ concentration at a given set of parameters θ and a specific time t, $[KHCO_3]^{exp}_{i\,(t)}$ (kmol/m^3) the experimental $KHCO_3$ concentration at the same time t, N_s the number of data points, and N_{ex} the number of experiments.

The ODEs (eqs 6, 7, and 9) are solved using the built-in MATLAB code "*ode45*", and the boundary conditions for the ODEs are $\mu_j = 0$ ($j = 0, 1, 2, ...$) and $C = C_0$ (initial prepared solution) at $t = 0$. According to Gómez et al.,[26] the initial value of θ selected is significant for the fitting of the parameters. Since the values are unknown, to reduce the possibility that the estimation falls into the local minimum values, a strategy of stochastic minimization using a build-in MATLAB code "*simulannealbnd*" was initially adopted. The values obtained from the above strategy were then set as the initial values of θ. A more rigorous method using built-in MATLAB code "*fmincon*" was then used to refine the evaluation of θ.

To check the robustness of model, a sensitivity analysis developed by Nagy et al.[27] was conducted to calculate the confidence intervals of the estimated parameters. By introducing ±1% disturbance on each parameter in θ, a sensitivity matrix on the ith parameter M_{θ_i} can be determined using central differences, which is given by

$$M_{\theta_i} = \frac{\partial [KHCO_3]^{sim}}{\partial \theta_i} \approx \frac{[KHCO_3]^{sim}_t(\theta_i^+) - [KHCO_3]^{sim}_t(\theta_i^-)}{2\Delta\theta_i} \quad i = 1, 2, ..., 5 \quad (17)$$

For one set of experiments in this case, since θ contains five parameters required to be estimated ($N_\theta = 5$), the sensitivity matrix has the scale of ($N_s \times N_\theta$). Considering that several experiments were conducted, the overall measurement matrix is given by

$$M_{\theta,Tol} = \begin{bmatrix} M_\theta{}^1 \\ M_\theta{}^2 \\ \vdots \\ M_\theta{}^{N_{ex}} \end{bmatrix} \quad (18)$$

The corresponding precision matrix P is determined by

$$P = (M^T_{\theta,Tol} M_{\theta,Tol})^{-1} \quad (19)$$

In this case, the total degrees of freedom (N_{df}) and residual variance ($s_R{}^2$) can be calculated as

$$N_{df} = \left(\sum_1^{N_{ex}} N_s\right) + 1 - N_\theta - 1 \quad (20)$$

$$s_R{}^2 = \frac{E}{N_{df}} \quad (21)$$

where E is obtained from eq 16.

Therefore, the covariance matrix (V) is determined by

$$V = s_R{}^2 P \quad (22)$$

The 95% confidence intervals can be obtained using t-test evaluation with $\alpha = 0.05$, which is given by

$$\theta = \theta^* \pm t_{\alpha/2,N_{df}} \sqrt{\mathrm{diag}(V)} \quad (23)$$

where θ^* represents regressed parameters, $t_{\alpha/2,\,N_{df}}$ is the t-distribution with a given N_{df} degrees of freedom.

4. RESULTS AND DISCUSSION

4.1. Solubility Measurement and Simulation. Considering the nonideal behavior of the K_2CO_3−$KHCO_3$−H_2O solvent system, activity coefficients are required.[28] In our previous work, the electrolyte nonrandom two-liquids activity coefficient model (ENRTL) was regressed against ~3000 experimental points in Aspen Plus (Version 8.6) to simulate the vapor−liquid−solid equilibrium (VLSE) thermodynamic properties of this ternary system. The regressed model was determined to be reasonable, with a deviation of ±4.2%.[11]

In the K_2CO_3−$KHCO_3$−H_2O solvent system, depending on the concentration of each component, there are generally three possible precipitates, including potassium carbonate (K_2CO_3), potassium bicarbonate ($KHCO_3$), and hydrated potassium carbonate ($K_2CO_3 \cdot 1.5H_2O$), as shown in reactions R2−R4.

$$K_2CO_3(s) \rightleftharpoons 2K^+(aq) + CO_3^{2-}(aq) \quad (R2)$$

$$KHCO_3(s) \rightleftharpoons K^+(aq) + HCO_3^-(aq) \quad (R3)$$

$$K_2CO_3 \cdot 1.5H_2O(s) \rightleftharpoons 2K^+(aq) + CO_3^{2-}(aq) + 1.5H_2O(l) \quad (R4)$$

The equilibrium constants for reactions R2−R4 can be expressed as a temperature-dependent equation, which is given by

$$\ln K_{(R_i)} = A_i + \frac{B_i}{T} + C_i \ln T + D_i T \qquad i = 2, 3, 4 \quad (24)$$

The coefficients for solid equilibrium constants in reactions R2−R4 were regressed using the Data Regression System (DRS) in Aspen Plus. For further details of the regression method and

DOI: 10.1021/acs.iecr.7b03637
Ind. Eng. Chem. Res. 2017, 56, 15131−15142

strategy, refer to the work of Hilliard[29] and Lee et al.[30] The coefficients are given in Table 3.

Table 3. Coefficients for Solid Equilibrium Constant[30]

reaction	A	B	C	D
R2	−176.00	17765.2	21.69	
R3	−274.72	9544.26	41.34	
R4	−270.15	−12266.1	−41.14	

The phase diagram of the ternary system under post-combustion CO_2 capture conditions can be simulated using the regressed ENRTL thermodynamic property model. The results are shown in Figure 4. Solubility experiments in the K_2CO_3−$KHCO_3$−H_2O solvent system at 18.75 °C were also conducted using the polythermal method to validate the ENRTL model.[31]

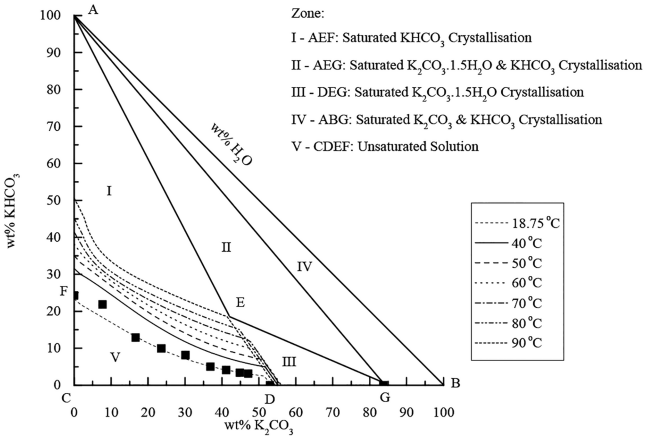

Figure 4. Simulated phase diagram of K_2CO_3−$KHCO_3$−H_2O system using Aspen Plus.

As indicated in Figure 4, for the concentrations and loadings used in this study, $KHCO_3$ (kalicinite) should be the only precipitate in the solvent system (Zone I). This has also been justified by Ye et al. and in our previous work.[9,11]

The solubility of 40 wt % apparent K_2CO_3 solvent with a loading of 0.4 at different temperatures has been measured and validated by the model (Figure 5). The consistent results as presented in Figures 4 and 5 indicate that the regressed ENRTL model is capable of predicting the solubility of the K_2CO_3−$KHCO_3$−H_2O solvent system under post-combustion CO_2 capture conditions.

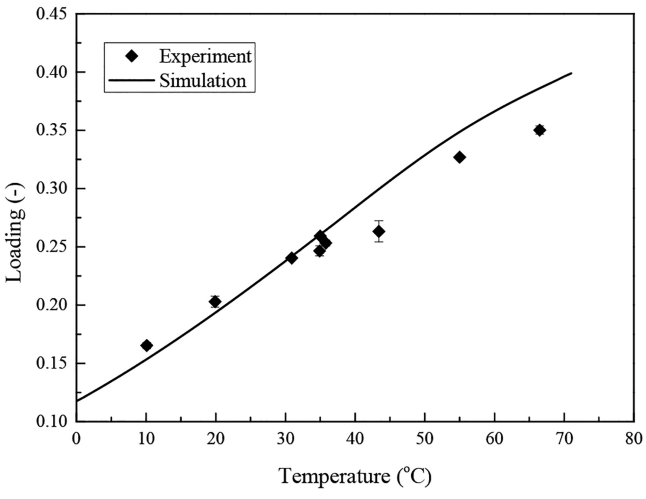

Figure 5. Experimental and simulated loading curve at 40 wt % apparent K_2CO_3 solvent.

4.2. Parameter Estimation and Validation for Crystallization Kinetics. As described, parameters were estimated using eq 16, combined with eqs 5−7, 9, and 10−13 in MATLAB, and the robustness of the parameters was evaluated using eqs 17−23. From Table 2, there are two groups of experiments including apparent K_2CO_3 concentrations of 35 and 40 wt %, both with a loading of 0.4. Considering that there are two primary nucleation mechanisms related to cooling rates in the unseeded batch crystallizer, the entire experimental design was divided into four subsets: (1) 35 wt % apparent K_2CO_3 concentration with homogeneous nucleation; (2) 35 wt % apparent K_2CO_3 concentration with heterogeneous nucleation; (3) 40 wt % apparent K_2CO_3 concentration with homogeneous nucleation; and (4) 40 wt % apparent K_2CO_3 concentration with heterogeneous nucleation. The purpose is to utilize a single set of parameters to predict the crystallization behaviors of the K_2CO_3−$KHCO_3$−H_2O solvent system across a spread of compositions and operating conditions.

The estimated parameters and their 95% confidential intervals are shown in Table 4, and the fitting results are shown in Figures 6−9.

Figures 6−9 show the fitting results for the concentration of dissolved $KHCO_3$ in the K_2CO_3−$KHCO_3$−H_2O solvent system with different compositions and primary nucleation mechanisms. The saturation temperature of each experiment was simulated using the regressed ENRTL model at the required composition (40 and 35 wt % apparent K_2CO_3 concentration with 0.4 loading). Time zero was set at the point that the solution equaled the saturated temperature, and the experiment was finished when the experiments reached the preset end temperature. Therefore, Figures 6−9 show curves that are horizontal at the beginning of each experiment, reflecting the induction time of the batch cooling crystallization experiment. After the induction period, the supersaturation of $KHCO_3$ is continuously consumed for primary nucleation, secondary nucleation, and crystal growth.

The regressed parameters shown in Table 4 indicate that the concentration of K_2CO_3 has a direct effect on the nucleation and growth of $KHCO_3$ crystals. This is reflected in the nucleation parameter k_1 and growth parameter g: both parameters in 40 wt % experiments are smaller than those in 35 wt % experiments. Much literature has mentioned that the growth exponential factor g is generally between 1 and 2; however, in reality, it is a characteristic of the crystallization system.[22] In some inorganic systems (barium nitrate, for example), Khamskij found that the growth exponential factor g was >10, because low supersaturation dominates crystal growth, leading to a high g.[21,32] This may be also applicable in our system as the supersaturation in the investigated range is low ($S < 1.3$), resulting in a high value of g in samples with an apparent K_2CO_3 concentration of 35 wt % with heterogeneous nucleation.

The secondary nucleation, in this case, may be suppressed by the primary nucleation, as the overall pro-exponential coefficient $k_2\mu_2$ ((number of crystals)/(m^3 of solvent)/min) of the secondary nucleation is several magnitudes smaller than the primary nucleation pre-exponential coefficient k_1 in all unseeded crystallization experiments. Therefore, primary nucleation dominates the nucleation of the K_2CO_3−$KHCO_3$−H_2O solvent system. In addition, since the primary nucleation can be classified as homogeneous nucleation and heterogeneous nucleation, depending on the cooling rates, it was found that, at the same

DOI: 10.1021/acs.iecr.7b03637
Ind. Eng. Chem. Res. 2017, 56, 15131−15142

Table 4. Regressed Parameters from Multiple Sets of Data in MATLAB

experimental number	k_1 (number of crystals)/(m^3 of solvent)/min)	B_1[a]	k_2 ($1/m^2$/min)	b_2	k_g (m/min)	g
			40 wt % Apparent K_2CO_3 Concentration, Heterogeneous Nucleation			
40W0.05R	$(3.317 \pm 0.010) \times 10^{11}$	0.00772	$(4.340 \pm 0.006) \times 10^{9}$	0.836 ± 0.016	$(1.195 \pm 0.0002) \times 10^{-5}$	3.200 ± 0.0006
40W0.1R	$(3.317 \pm 0.010) \times 10^{11}$	0.00772	$(4.340 \pm 0.006) \times 10^{9}$	0.836 ± 0.016	$(1.195 \pm 0.0002) \times 10^{-5}$	3.200 ± 0.0006
40W0.25R	$(3.317 \pm 0.010) \times 10^{11}$	0.00772	$(4.340 \pm 0.006) \times 10^{9}$	0.836 ± 0.016	$(1.195 \pm 0.0002) \times 10^{-5}$	3.200 ± 0.0006
40W0.5R	$(3.317 \pm 0.010) \times 10^{11}$	0.00772	$(4.340 \pm 0.006) \times 10^{9}$	0.836 ± 0.016	$(1.195 \pm 0.0002) \times 10^{-5}$	3.200 ± 0.0006
			40 wt % Apparent K_2CO_3 Concentration, Homogeneous Nucleation			
40W0.75R_1	$(1.201 \pm 0.010) \times 10^{12}$	0.00104	$(3.227 \pm 0.019) \times 10^{10}$	0.145 ± 0.024	$(1.466 \pm 0.003) \times 10^{-6}$	1.177 ± 0.012
40W0.75R_2	$(1.201 \pm 0.010) \times 10^{12}$	0.00104	$(3.227 \pm 0.019) \times 10^{10}$	0.145 ± 0.024	$(1.466 \pm 0.003) \times 10^{-6}$	1.177 ± 0.012
			35 wt % Apparent K_2CO_3 Concentration, Heterogeneous Nucleation			
35W0.1R	$(1.854 \pm 0.020) \times 10^{12}$	0.00558	$(4.598 \pm 0.0001) \times 10^{12}$	0.932 ± 0.032	$(4.598 \pm 0.013) \times 10^{-5}$	4.355 ± 0.004
35W0.25R	$(1.854 \pm 0.020) \times 10^{12}$	0.00558	$(4.598 \pm 0.0001) \times 10^{12}$	0.932 ± 0.032	$(4.598 \pm 0.013) \times 10^{-5}$	4.355 ± 0.004
35W0.5R	$(1.854 \pm 0.020) \times 10^{12}$	0.00558	$(4.598 \pm 0.0001) \times 10^{12}$	0.932 ± 0.032	$(4.598 \pm 0.013) \times 10^{-5}$	4.355 ± 0.004
			35 wt % Apparent K_2CO_3 Concentration, Homogeneous Nucleation			
35W0.75R	$(2.282 \pm 0.102) \times 10^{12}$	0.00253	$(2.471 \pm 0.116) \times 10^{12}$	1.995 ± 0.071	$(3.745 \pm 0.006) \times 10^{-7}$	3.746 ± 0.014
35W1R	$(2.282 \pm 0.102) \times 10^{12}$	0.00253	$(2.471 \pm 0.116) \times 10^{12}$	1.995 ± 0.071	$(3.745 \pm 0.006) \times 10^{-7}$	3.746 ± 0.014

[a]The values are fixed from Table 2.

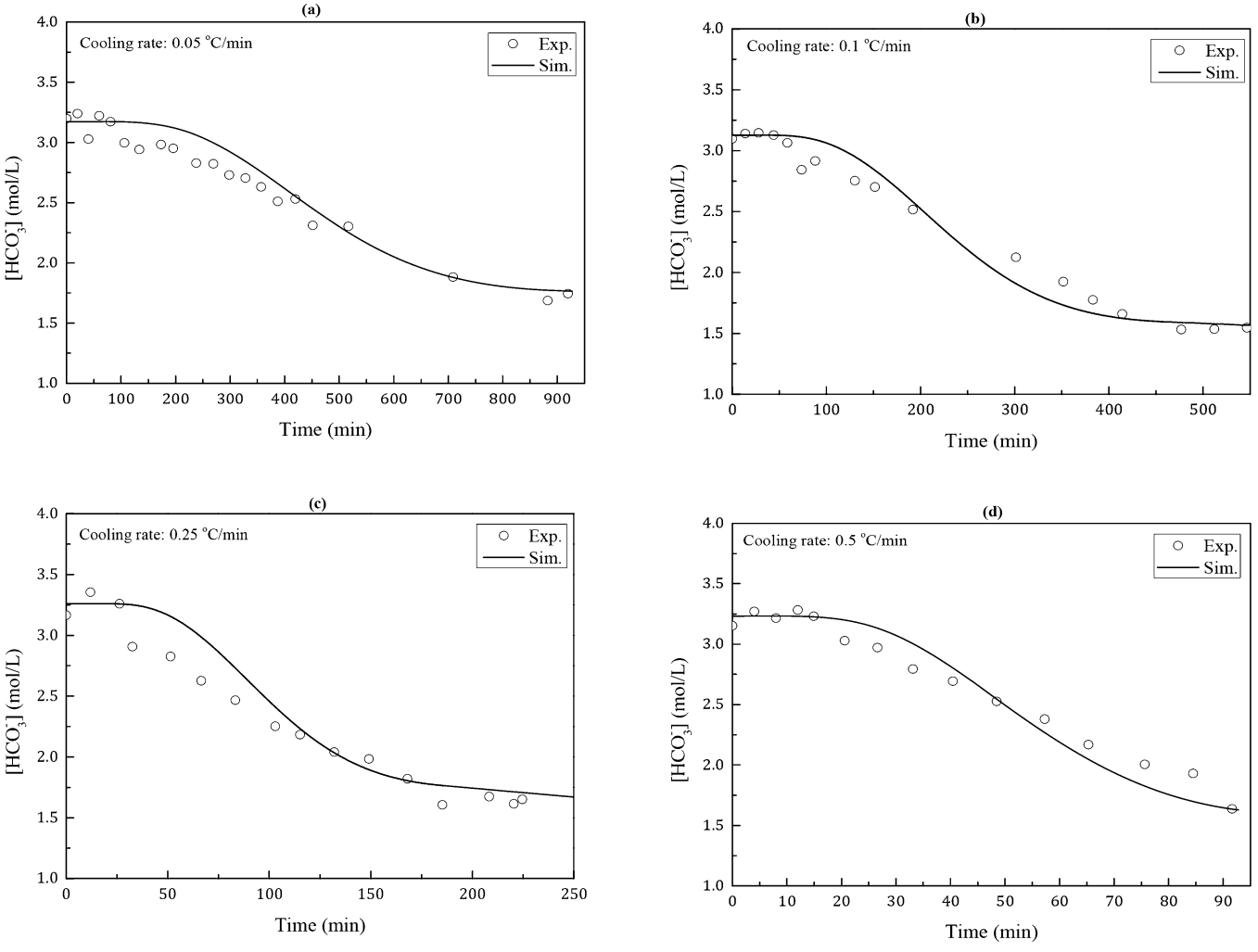

Figure 6. Fittings of experimental data in 40 wt % K_2CO_3 concentration, with 0.4 loading and heterogeneous nucleation: (a) 40W0.05R, (b) 40W0.1R, (c) 40W0.25R, and (d) 40W0.5R.

apparent K_2CO_3 concentration, the experiments at low cooling rates (heterogeneous) have a lower k_1 than those at high cooling rates (homogeneous). The growth coefficients (k_g and g) at low cooling rates are higher than those at high cooling rates. It was observed that, at higher cooling rates, more $KHCO_3$ crystals with a smaller size were precipitated as homogeneous nucleation occurred at high supersaturation and the growth was inhibited accordingly, because of the large consumption for the nucleation.

DOI: 10.1021/acs.iecr.7b03637
Ind. Eng. Chem. Res. 2017, 56, 15131−15142

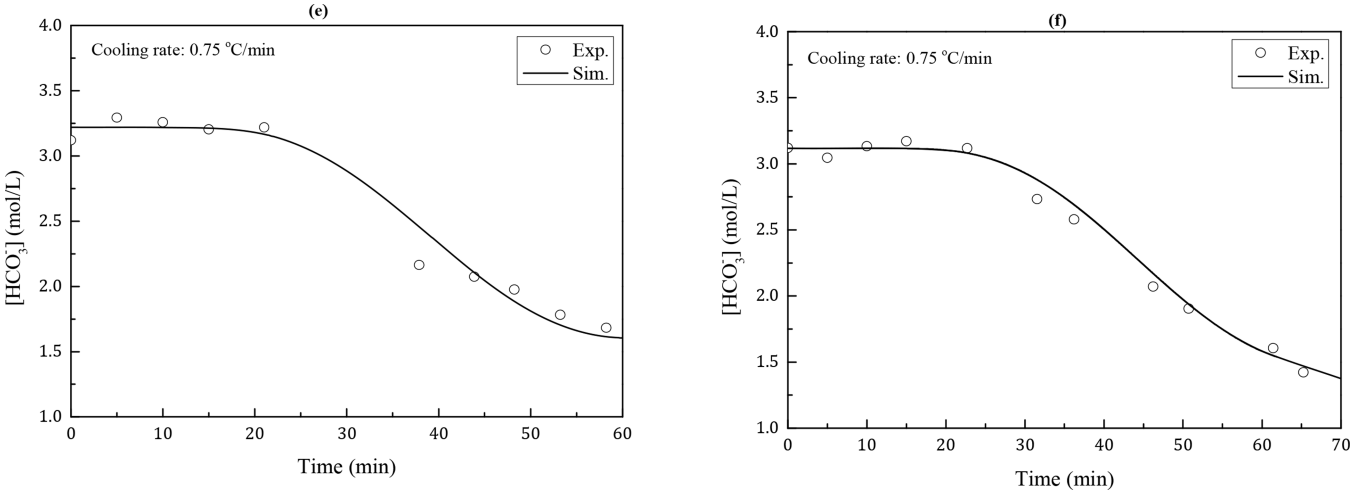

Figure 7. Fittings of experimental data in 40 wt % K_2CO_3 concentration, with 0.4 loading and homogeneous nucleation: (e) 40W0.75R_1 and (f) 40W0.75R_2.

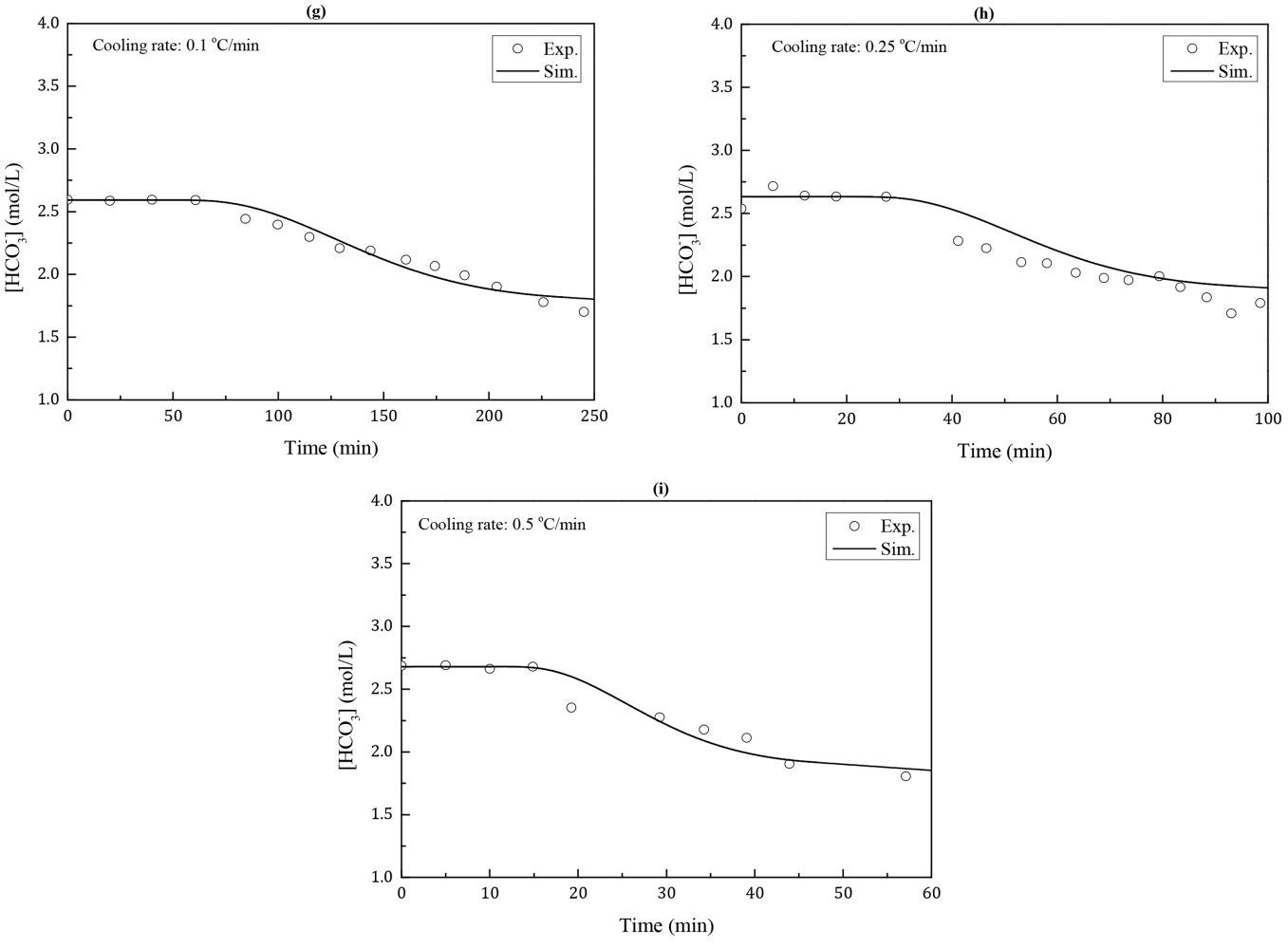

Figure 8. Fittings of experimental data in 35 wt % K_2CO_3 concentration, with 0.4 loading and heterogeneous nucleation: (g) 35W0.1R, (h) 35W0.25R, and (i) 35W0.5R).

In contrast, less $KHCO_3$ crystals with larger size were found in heterogeneous nucleation and growth.

From the robustness analysis, the parameters have reasonable confidence intervals. According to Gómez et al.,[26] compared a single-experiment fitting, with the introduction of multiple-experiment data into the regression strategy simultaneously, the parameter estimation becomes more reliable and robust, and there is less opportunity for the estimation to be trapped in a local minimum. Here, 11 different batch experiments were used to explain the crystallization behaviors in the K_2CO_3−$KHCO_3$−H_2O solvent system. To validate the parameter estimation, two more experiments (35 wt % apparent K_2CO_3 concentration, with

DOI: 10.1021/acs.iecr.7b03637
Ind. Eng. Chem. Res. 2017, 56, 15131−15142

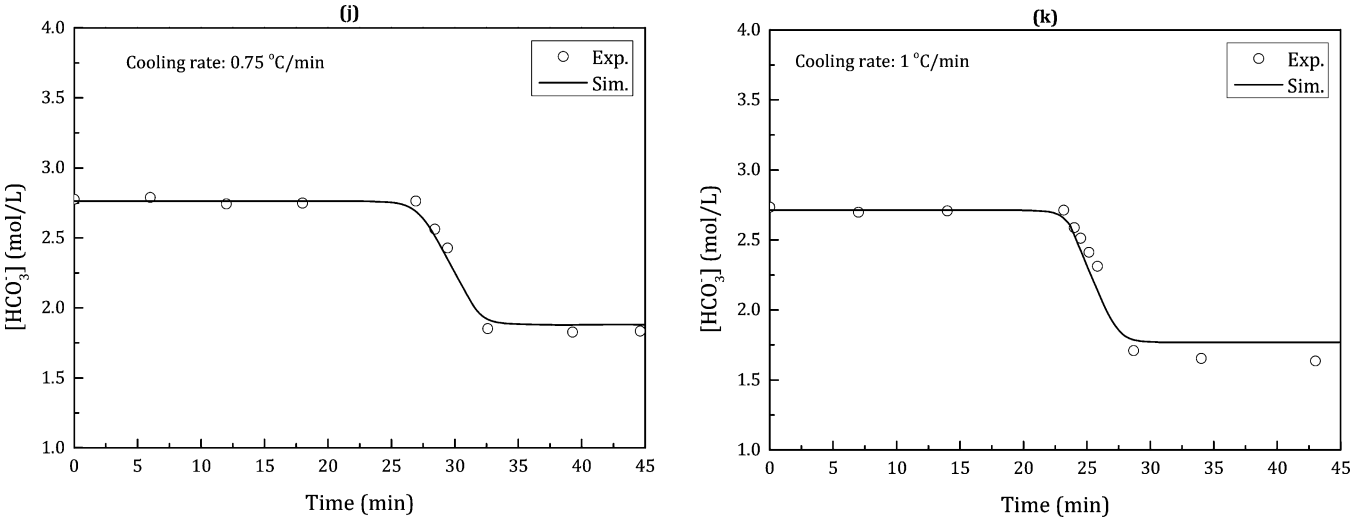

Figure 9. Fittings of experimental data in 35 wt % K_2CO_3 concentration, with 0.4 loading and homogeneous nucleation: (j) 35W0.75R and (k) 35W1R.

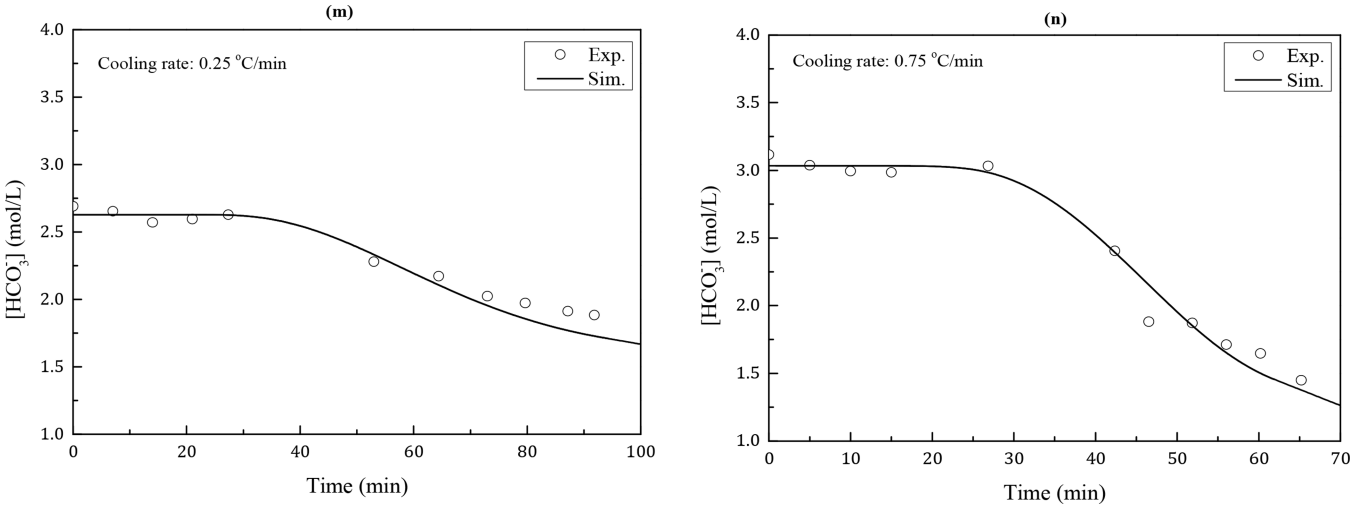

Figure 10. Validation of the simulation ((m) 35 wt % K_2CO_3 concentration at 0.25 °C/min and (n) 40 wt % K_2CO_3 concentration at 0.75 °C/min).

0.4 loading, at a cooling rate of 0.25 °C/min; and 40 wt % apparent K_2CO_3 concentration, with 0.4 loading, at a cooling rate of 0.75 °C/min) were conducted, and the results were compared with the modeling with the estimated parameters, which is shown in Figure 10. The model was determined to be consistent with the experimental data.

4.3. Approximation of Crystal Mean Size. Since the parameters were only regressed from the $KHCO_3$ concentration profile (eq 16), there is a risk that the corresponding particle size distribution may not be predicted by the model. In addition, chord length distribution (CLD) may not actually reflect the real particle size distribution (CSD). Wang and co-workers[34] and Trifovic et al.[33] directly used the chord length distribution to determine the crystallization kinetics in their system. However, the fit was relatively poor. Other works studied the relationship between CSD and CLD using first-principles. In these works, the geometric model required several assumptions, such as a uniform shape and opaque facet of crystals, which is highly dependent on the crystallization system.[35,36] Here, a strategy of mapping the CSD moments and the CLD moments developed by Kee, Braatz, and co-workers was used, based on the assumption that the mapping relationship is static and can be treated as a "*gray box*".[19]

Therefore, in our system, at any moment of the experiment, there is a mass balance, which can be given by

$$C_{0,\mathrm{KHCO_3}} V_{0,\mathrm{sol}} = (\mu_3 \rho_c k_v + C_{\mathrm{KHCO_3}}) V_{\mathrm{sol}} \tag{25}$$

where $C_{0,\mathrm{KHCO_3}}$ (kmol/m^3) and $V_{0,\mathrm{sol}}$ (m^3) are the initial concentration of $KHCO_3$ and the initial solvent volume, respectively. $C_{\mathrm{KHCO_3}}$ (kmol/m^3) and V_{sol} (m^3) are the in situ concentration of $KHCO_3$ and the in situ solvent volume, respectively.

As the CLD is a logarithmic normal distribution, the jth CLD moments (μ_j^c) measured by FBRM can be determined as

$$\mu_j^c = \sum_{i=1}^{N-1} (\sqrt{L_i^c L_{i+1}^c})^j n^c_{(L_{i+1}^c - L_i^c)} \qquad (j = 0, 1, 2, 3, 4, \ldots) \tag{26}$$

where L_i (m) and L_{i+1} (m) are the chord length boundaries of default channels in FBRM (the minimum chord length L_1 is 1 μm, and the maximum chord length L_N is 1000 μm), $n^c_{(L_{i+1}^c - L_i^c)}$ (the number of counts) is the chord length population balance in a specific channel.

Each order of CLD moments, μ_j^c, was calculated using eq 26 and scaled, in order to fit the third CSD moment μ_3. A higher

DOI: 10.1021/acs.iecr.7b03637
Ind. Eng. Chem. Res. 2017, 56, 15131−15142

order of the CLD moments (μ_4^c) has the best agreement with μ_3, which is shown in Figure 11, and, thus, the mapping relationship is given by

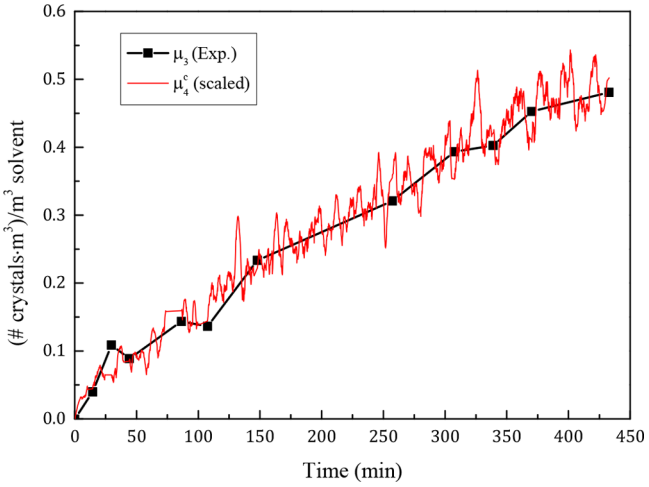

Figure 11. Fitting of the CLD moment μ_4^c with the CSD moment μ_3.

$$\mu_j = \varphi_j \mu_{j+1}^c \tag{27}$$

where φ_j ((number of crystals·min/(number of counts)/m/(m^3 of solvent)) is the mapping coefficient.

This higher order of the CLD moments mapping relationship can be found in all of the experiments. Previous studies that investigated the relationship between CLD moments and CSD moments also found that the mapping relationship was case-dependent. A lower-order relationship ($\mu_j = \gamma_j \mu_{j-1}^c$) has been found by Wynn[38] and Morbidelli et al.,[37] an equal-order relationship ($\mu_j = \lambda_j \mu_j^c$) has been found by Luo et al.,[39] and a higher-order relationship ($\mu_j = \lambda_j \mu_{j+1}^c$) which is commonly used in an industrial practice called "length-weighting", has been found in the work of Braatz.[19] The last relationship is the same with our work.

Further tests on particle size were conducted by checking the final volume-based average chord length moments of each experiment, which is given by

$$\bar{L}_{\mathrm{CLD}} = \sum_{i=1}^{N_s} \frac{\mu_{4,i}^c}{\mu_{3,i}^c} \tag{28}$$

By introducing the static mapping coefficient, the final average particle size of each experiment can be determined by

$$\bar{L}_{\mathrm{CSD}}^{\mathrm{exp}} = \varphi_{\mathrm{exp}} \bar{L}_{\mathrm{CLD}} \tag{29}$$

Since a higher order exists in this case, the final area-based average CSD moments simulated in the model can be calculated as

$$\bar{L}_{\mathrm{CSD}}^{\mathrm{sim}} = \frac{\mu_{3,\mathrm{end}}}{\mu_{2,\mathrm{end}}} \tag{30}$$

The comparison results between $\bar{L}_{\mathrm{CSD}}^{\mathrm{exp}}$ and $\bar{L}_{\mathrm{CSD}}^{\mathrm{sim}}$ in each experiment are listed in Table 5 and Figure 12.

Figure 12 shows that the final average particle size measured by FBRM in all experiments fit the modeling results well, within an error of 20%. The final average particle size from the group of experiments with an apparent K_2CO_3 concentration of 35 wt % has a clear boundary, depending on the different primary nucleation mechanisms, and the results in Table 5 are in agreement with

Table 5. Final Average Particle Size Obtained from the CLD Moments and the CSD Moments

	Final Average Particle Size (μm)	
experiment No.	experiment	simulation
35W0.1R	8.180	6.882
35W0.25R	9.439	8.655
35W0.5R	9.229	9.895
35W0.75R	0.807	0.871
35W1R	0.714	0.873
40W0.05R	29.980	27.684
40W0.1R	26.455	29.649
40W0.25R	42.988	34.422
40W0.5R	41.664	39.837
40W0.75R_1	28.117	24.607
40W0.75R_2	27.845	23.921
35W0.25R_validation	10.203	8.223
40W0.75R_validation	28.289	24.049

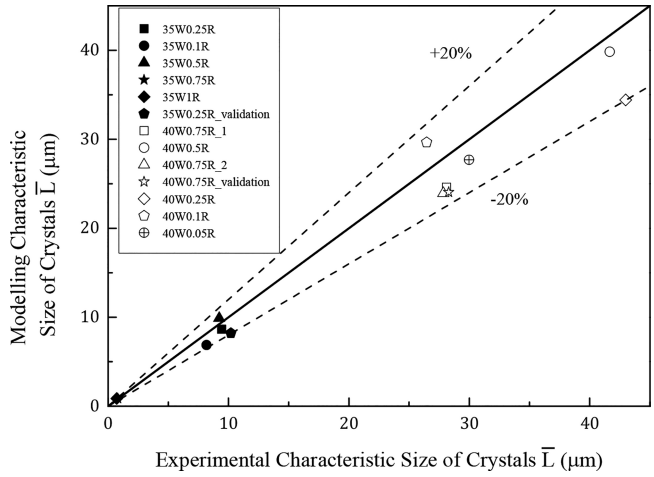

Figure 12. Comparison of final average particle size between experiment and simulation.

the conclusions drawn from the parameter estimation. That is, the system with homogeneous nucleation has more particles with smaller size, because of the slow growth rate, whereas the system with heterogeneous nucleation has less particles with larger size, thus having a bigger average particle size. For the group of experiments with 40 wt % apparent K_2CO_3 concentration, it is also found that the average particle size with heterogeneous nucleation is generally larger than that observed with homogeneous nucleation. However, the experiments with heterogeneous nucleation (40W0.05R, 40W0.1R, 40W0.25R, 40W0.5R) do not have similar particle size, compared to the other group with heterogeneous nucleation. A possible reason may be that, at low cooling rates, in the range between 0.1 °C/min and 0.05 °C/min, the generation of supersaturation is affected by the high concentration of aqueous K_2CO_3. This slows the crystal growth rate, thus having a relatively smaller particle size, compared to the experiments with 0.25 °C/min and 0.5 °C/min cooling rates. In addition, the overall particle size in the group with an apparent K_2CO_3 concentration of 35 wt % is smaller than that with an apparent K_2CO_3 concentration of 40 wt %, possibly due to the low initial concentration of $KHCO_3$.

5. CONCLUSION

The crystallization kinetics including primary nucleation, secondary nucleation, and growth rate of the K_2CO_3−$KHCO_3$−H_2O

DOI: 10.1021/acs.iecr.7b03637
Ind. Eng. Chem. Res. 2017, 56, 15131−15142

solvent system have been systematically investigated in unseeded batch cooling crystallization experiments. By taking advantage of the method of moments, the parameters for the crystallization kinetics have been estimated using a regression strategy with a stochastic minimization, followed by a deterministic minimization. The 95% confidential intervals were obtained through a robustness evaluation method combining with multiple-experiment data. Under post-combustion conditions and selected solvent concentrations with loadings, $KHCO_3$ was the only precipitate in this ternary solvent system, and the solubility of $KHCO_3$ can be predicted confidently using the regressed ENRTL model.

The chord length distribution measured by FBRM can provide a reasonable prediction on final average particle size using a high order of mapping relationship with the particle size distribution moments. There are two primary nucleation types exhibited, including homogeneous nucleation at high constant cooling rates and heterogeneous nucleation at low constant cooling rates in the ternary solvent system, and the secondary nucleation was found inhibited in all experiments. Both the supersaturation of $KHCO_3$ and K_2CO_3 affect the nucleation and growth rate of $KHCO_3$ crystals. More particles with smaller size are formed in homogeneous nucleation, whereas less particles with larger size are formed in heterogeneous nucleation, which has been captured by FBRM measurement and the regressed model. The model combined with FBRM measurement is applicable to predict the crystallization kinetics in the K_2CO_3–$KHCO_3$–H_2O solvent system.

AUTHOR INFORMATION

Corresponding Author

*Tel.: +61 3 83440048. Fax: +61 3 83444153. E-mail: mumfordk@unimelb.edu.au.

ORCID

Geoffrey W. Stevens: 0000-0002-5788-4682

Kathryn A. Mumford: 0000-0002-7056-5600

Notes

The authors declare no competing financial interest.

ACKNOWLEDGMENTS

The authors acknowledge the financial support from Peter Cook Centre for CCS Research and the infrastructure support from the Particulate Fluids Processing Centre (PFPC), a special research centre of the Australian Research Council.

REFERENCES

(1) Benson, H. E.; Field, J. H.; Jimeson, R. M. CO_2 Absorption Employing Hot Potassium Carbonate Solutions. *Chem. Process Eng.* **1954**, *50*, 356–364.

(2) Shen, S.; Feng, X.; Zhao, R.; Ghosh, U. K.; Chen, A. Kinetic Study of Carbon Dioxide Absorption with Aqueous Potassium Carbonate Promoted by Arginine. *Chem. Eng. J.* **2013**, *222*, 478–487.

(3) Aronu, U. E.; Svendsen, H. F.; Hoff, K. A. Investigation of Amine Amino Acid Salts for Carbon Dioxide Absorption. *Int. J. Greenhouse Gas Control* **2010**, *4* (5), 771–775.

(4) Lim, J.; Aguiar, A.; Scholes, C. A.; Dumée, L. F.; Stevens, G. W.; Kentish, S. E. Monoethanolamine Reclamation Using Electrodialysis. *Ind. Eng. Chem. Res.* **2014**, *53* (49), 19313–19321.

(5) Hu, G.; Smith, K. H.; Wu, Y.; Kentish, S. E.; Stevens, G. W. Screening Amino Acid Salts as Rate Promoters in Potassium Carbonate Solvent for Carbon Dioxide Absorption. *Energy Fuels* **2017**, *31* (4), 4280–4286.

(6) Hu, G.; Nicholas, N. J.; Smith, K. H.; Mumford, K. A.; Kentish, S. E.; Stevens, G. W. Carbon Dioxide Absorption into Promoted Potassium Carbonate Solutions: A Review. *Int. J. Greenhouse Gas Control* **2016**, *53*, 28–40.

(7) Mumford, K. A.; Wu, Y.; Smith, K. H.; Stevens, G. W. Review of Solvent Based Carbon-Dioxide Capture Technologies. *Front. Chem. Sci. Eng.* **2015**, *9* (2), 125–141.

(8) Smith, K.; Xiao, G.; Mumford, K.; Gouw, J.; Indrawan, I.; Thanumurthy, N.; Quyn, D.; Cuthbertson, R.; Rayer, A.; Nicholas, N.; Lee, A.; da Silva, G.; Kentish, S.; Harkin, T.; Qader, A.; Anderson, C.; Hooper, B.; Stevens, G. Demonstration of a Concentrated Potassium Carbonate Process for CO_2 Capture. *Energy Fuels* **2014**, *28* (1), 299–306.

(9) Ye, Q.; Wang, X.; Lu, Y. Kinetic Behavior of Potassium Bicarbonate Crystallization in a Carbonate-Based CO_2 Absorption Process. *Chem. Eng. Res. Des.* **2015**, *93*, 136–147.

(10) Li, H.; Kawajiri, Y.; Grover, M. A.; Rousseau, R. W. Modeling of Nucleation and Growth Kinetics for Unseeded Batch Cooling Crystallization. *Ind. Eng. Chem. Res.* **2017**, *56* (14), 4060–4073.

(11) Wu, Y.; Mirza, N. R.; Hu, G.; Smith, K. H.; Stevens, G. W.; Mumford, K. A. Precipitating Characteristics of Potassium Bicarbonate Using Concentrated Potassium Carbonate Solvent for Carbon Dioxide Capture. Part 1. *Ind. Eng. Chem. Res.* **2017**, *56* (23), 6764–6774.

(12) Wappel, D.; Joswig, S.; Khan, A. A.; Smith, K. H.; Kentish, S. E.; Shallcross, D. C.; Stevens, G. W. The Solubility of Sulfur Dioxide and Carbon Dioxide in an Aqueous Solution of Potassium Carbonate. *Int. J. Greenhouse Gas Control* **2011**, *5* (6), 1454–1459.

(13) Kadam, S. S.; Kramer, H. J. M.; ter Horst, J. H. Combination of a Single Primary Nucleation Event and Secondary Nucleation in Crystallization Processes. *Cryst. Growth Des.* **2011**, *11* (4), 1271–1277.

(14) Mohameed, H. A.; Abu-Jdayil, B.; Al Khateeb, M. Effect of Cooling Rate on Unseeded Batch Crystallization of KCl. *Chem. Eng. Process.* **2002**, *41* (4), 297–302.

(15) Zhao, X.; Smith, K. H.; Simioni, M. A.; Tao, W.; Kentish, S. E.; Fei, W.; Stevens, G. W. Comparison of Several Packings for CO_2 Chemical Absorption in a Packed Column. *Int. J. Greenhouse Gas Control* **2011**, *5* (5), 1163–1169.

(16) Qian, Y.; Lu, G.; Sun, Y.; Song, X.; Yu, J. Modeling of Strontium Chloride Hexahydrate Growth during Unseeded Batch Cooling Crystallization by Two-Dimensional Population Balance Equation. *CrystEngComm* **2015**, *17* (48), 9394–9403.

(17) Wang, Y.; Smith, K. H.; Mumford, K.; Grabin, T. F.; Li, Z.; Stevens, G. W. Prediction of Dispersed Phase Holdup in Pulsed Disc and Doughnut Solvent Extraction Columns under Different Mass Transfer Conditions. *Chin. J. Chem. Eng.* **2016**, *24* (2), 226–231.

(18) Gherras, N.; Fevotte, G. On the Use of Process Analytical Technologies and Population Balance Equations for the Estimation of Crystallization Kinetics. *AIChE J.* **2012**, *58* (9), 2650–2664.

(19) Kee, N. C. S.; Arendt, P. D.; May Goh, L.; Tan, R. B. H.; Braatz, R. D. Nucleation and Growth Kinetics Estimation for L-Phenylalanine Hydrate and Anhydrate Crystallization. *CrystEngComm* **2011**, *13* (4), 1197.

(20) Randolph, A. D.; Larson, M. A. *Theory of Particulate Processes: Analysis and Techniques of Continuous Crystallization*; Academic Press: San Diego, CA, 1988.

(21) Myerson, A. S. *Handbook of Industrial Crystallization*; Butterworth–Heinemann: Oxford, U.K., Boston, 2002.

(22) Mullin, J. W. *Crystallization*; Butterworth–Heinemann: Melbourne, Australia, Boston, 2001.

(23) Sangwal, K. A Novel Self-Consistent Nývlt-like Equation for Metastable Zone Width Determined by the Polythermal Method. *Cryst. Res. Technol.* **2009**, *44* (3), 231–247.

(24) Wey, J. S.; Estrin, J. Modeling the Batch Crystallization Process. The Ice–Brine System. *Ind. Eng. Chem. Process Des. Dev.* **1973**, *12* (3), 236–246.

(25) Yu, Z. Q.; Chow, P. S.; Tan, R. B. H. Interpretation of Focused Beam Reflectance Measurement (FBRM) Data via Simulated Crystallization. *Org. Process Res. Dev.* **2008**, *12* (4), 646–654.

(26) Encarnación-Gómez, L. G.; Bommarius, A. S.; Rousseau, R. W. Crystallization Kinetics of Ampicillin Using Online Monitoring Tools

DOI: 10.1021/acs.iecr.7b03637
Ind. Eng. Chem. Res. 2017, 56, 15131–15142

and Robust Parameter Estimation. *Ind. Eng. Chem. Res.* **2016**, *55* (7), 2153−2162.
(27) Nagy, Z. K.; Fujiwara, M.; Woo, X. Y.; Braatz, R. D. Determination of the Kinetic Parameters for the Crystallization of Paracetamol from Water Using Metastable Zone Width Experiments. *Ind. Eng. Chem. Res.* **2008**, *47* (4), 1245−1252.
(28) Hilliard, M. D.; Rochelle, G. T. Thermodynamics of Aqueous Piperazine/potassium Carbonate/carbon Dioxide Chare Cterized by the Electrolyte Non-Random Two-Liquid Model in Aspen plus. *In Greenhouse Gas Control Technologies* **2005**, *II*, 1975−1978.
(29) Hilliard, M. D. A. Predictive Thermodynamic Model for an Aqueous Blend of Potassium Carbonate, Piperazine, and Monoethanolamine for Carbon Dioxide Capture from Flue Gas. Ph.D. Thesis, The University of Texas at Austin, Austin, TX, 2008.
(30) Lee, A.; Mumford, K. A.; Wu, Y.; Nicholas, N.; Stevens, G. W. Understanding the Vapour−liquid Equilibrium of CO_2 in Mixed Solutions of Potassium Carbonate and Potassium Glycinate. *Int. J. Greenhouse Gas Control* **2016**, *47*, 303−309.
(31) Fevotte, G.; Gherras, N.; Moutte, J. Batch Cooling Solution Crystallization of Ammonium Oxalate in the Presence of Impurities: Study of Solubility, Supersaturation, and Steady-State Inhibition. *Cryst. Growth Des.* **2013**, *13* (7), 2737−2748.
(32) Khamskij, E. V. On Certain Dependences of the Crystallization Rate of Supersaturation of a Solution. *Krist. Tech.* **1973**, *8* (1−3), 107−113.
(33) Trifkovic, M.; Sheikhzadeh, M.; Rohani, S. Kinetics Estimation and Single and Multi-Objective Optimization of a Seeded, Anti-Solvent, Isothermal Batch Crystallizer. *Ind. Eng. Chem. Res.* **2008**, *47* (5), 1586−1595.
(34) Zhang, Y.; Jiang, Y.; Zhang, D.; Qian, Y.; Wang, X. Z. Metastable Zone Width, Crystal Nucleation and Growth Kinetics Measurement in Anti-Solvent Crystallization of β-Artemether in the Mixture of Ethanol and Water. *Chem. Eng. Res. Des.* **2015**, *95* (2), 187−194.
(35) Hermanto, M. W.; Chow, P. S.; Tan, R. B. H. Operating Strategy to Produce Consistent CSD in Combined Antisolvent-Cooling Crystallization Using FBRM. *Ind. Eng. Chem. Res.* **2012**, *51* (42), 13773−13783.
(36) Li, H.; Kawajiri, Y.; Grover, M. A.; Rousseau, R. W. Application of an Empirical FBRM Model to Estimate Crystal Size Distributions in Batch Crystallization. *Cryst. Growth Des.* **2014**, *14* (2), 607−616.
(37) Vaccaro, A.; Šefčík, J.; Morbidelli, M. Modeling Focused Beam Reflectance Measurement and Its Application to Sizing of Particles of Variable Shape. *Part. Part. Syst. Charact.* **2006**, *23* (5), 360−373.
(38) Wynn, E. J. Relationship between Particle-Size and Chord-Length Distributions in Focused Beam Reflectance Measurement: Stability of Direct Inversion and Weighting. *Powder Technol.* **2003**, *133* (1−3), 125−133.
(39) Luo, Y. H.; Wu, G. G.; Sun, B. W. Antisolvent Crystallization of Biapenem: Estimation of Growth and Nucleation Kinetics. *J. Chem. Eng. Data* **2013**, *58* (3), 588−597.

DOI: 10.1021/acs.iecr.7b03637
Ind. Eng. Chem. Res. 2017, 56, 15131−15142